Development of MQXF: The Nb_3Sn Low-β Quadrupole for the HiLumi LHC

P. Ferracin, G. Ambrosio, M. Anerella, A. Ballarino, H. Bajas, M. Bajko, B. Bordini, R. Bossert, D. W. Cheng, D. R. Dietderich, G. Chlachidze, L. Cooley, H. Felice, A. Ghosh, R. Hafalia, E. Holik, S. Izquierdo Bermudez, P. Fessia, P. Grosclaude, M. Guinchard, M. Juchno, S. Krave, F. Lackner, M. Marchevsky, V. Marinozzi, F. Nobrega, L. Oberli, H. Pan, J. C. Perez, H. Prin, J. Rysti, E. Rochepault, G. Sabbi, T. Salmi, J. Schmalzle, M. Sorbi, S. Sequeira Tavares, E. Todesco, P. Wanderer, X. Wang, and M. Yu

(Invited Paper)

***Abstract*—The High Luminosity (HiLumi) Large Hadron Collider (LHC) project has, as the main objective, to increase the LHC peak luminosity by a factor five and the integrated luminosity by a factor ten. This goal will be achieved mainly with a new interaction region layout, which will allow a stronger focusing of the colliding beams. The target will be to reduce the beam size in the interaction points by a factor of two, which requires doubling the aperture of the low-β (or inner triplet) quadrupole magnets. The use of Nb_3Sn superconducting material and, as a result, the possibility of operating at magnetic field levels in the windings higher than 11 T will limit the increase in length of these quadrupoles, called MQXF, to acceptable levels. After the initial design phase, where the key parameters were chosen and the magnet's conceptual design finalized, the MQXF project, a joint effort between the U.S. LHC Accelerator Research Program and the Conseil Européen pour la Recherche Nucléaire (CERN), has now entered the construction and test phase of the short models. Concurrently, the preparation for the development of the full-length prototypes has been initiated. This paper will provide an overview of the project status, describing and reporting on the performance of the superconducting material, the lessons learnt during the fabrication of superconducting coils and support structure, and the fine tuning of the magnet design in view of the start of the prototyping phase.**

Manuscript received October 19, 2015; accepted December 14, 2015. Date of publication December 18, 2015; date of current version January 11, 2016. This work was supported in part by the EU FP7 High Luminosity (HiLumi) Large Hadron Collider (LHC) under Grant Agreement 284404 and by the DOE through the U.S. LHC Accelerator Research Program.

P. Ferracin, A. Ballarino, H. Bajas, M. Bajko, B. Bordini, S. Izquierdo Bermudez, P. Fessia, P. Grosclaude, M. Guinchard, M. Juchno, F. Lackner, L. Oberli, J. C. Perez, H. Prin, J. Rysti, E. Rochepault, S. Sequeira Tavares, and E. Todesco are with the Conseil Européen pour la Recherche Nucléaire (CERN), 1211 Geneva, Switzerland (e-mail: paolo.ferracin@cern.ch).

G. Ambrosio, R. Bossert, G. Chlachidze, L. Cooley, E. Holik, S. Krave, F. Nobrega, and M. Yu are with the Fermi National Accelerator Laboratory, Batavia, IL 80510 USA.

M. Anerella, A. Ghosh, J. Schmalzle, and P. Wanderer are with the Brookhaven National Laboratory, Upton, NY 11973 USA.

D. W. Cheng, D. R. Dietderich, H. Felice, R. Hafalia, M. Marchevsky, H. Pan, G. Sabbi, and X. Wang are with the Lawrence Berkeley National Laboratory, Berkeley, CA 94720 USA.

V. Marinozzi and M. Sorbi are with the Istituto Nazionale di Fisica Nucleare (INFN) Laboratorio Acceleratori e Superconduttività Applicata (LASA), 20090 Segrate, Italy.

T. Salmi is with the Tampere University of Technology, 33720 Tampere, Finland.

Color versions of one or more of the figures in this paper are available online at http://ieeexplore.ieee.org.

Digital Object Identifier 10.1109/TASC.2015.2510508

***Index Terms*—High Luminosity Large Hadron Collider (LHC), interaction regions, low-β quadrupoles, Nb_3Sn magnets.**

I. Introduction

In early October 2015, the Large Hadron Collider (LHC) has been operating at the energy of 6.5 TeV per beam, and has gathered 2 fb^{-1} of integrated luminosity with $4 \cdot 10^{33}$ $cm^{-2}s^{-1}$ peak luminosity. In the period 2015–2023, the LHC is then expected to reach a peak luminosity of $2 \cdot 10^{34}$ $cm^{-2}s^{-1}$, and an integrated luminosity of 300 fb^{-1}, with a possible increase of energy to 7 TeV per beam. With the HiLumi Project, CERN is planning to upgrade the Interaction Region in the period 2024–2026 in order to achieve a peak luminosity of $5 \cdot 10^{34}$ $cm^{-2}s^{-1}$, and to reach 3000 fb^{-1} integrated luminosity in about 12 years after the upgrade [1].

Among the components to be upgraded are the inner triplet (or low-β) quadrupole magnets, denoted as Q1, Q2a, Q2b, and Q3. In the present LHC, the triplet quadrupoles use Nb-Ti superconducting coils to generate a gradient of 215 T/m in a 70 mm aperture, with a magnetic length of 6.3 m for Q1 and Q3 [2], and 5.5 m for Q2a and Q2b [3], and with a conductor peak field of 7.7 and 8.6 T, respectively. The new triplet magnets, call ed MQXF (see Fig. 1), will feature an aperture of 150 mm, and, by relying on Nb_3Sn superconductor, will operate at a gradient of 132.6 T/m and a conductor peak field of 11.4 T. A schematic view of the new interaction region is provided in Fig. 2: two magnets, called MQXFA and with a magnetic length of 4.2 m, will be inserted in the same cold-mass and cryostat (thin black boxes) for the Q1 and Q3 quadrupoles; one magnet, called MQXFB and with a magnetic length of 7.15 m, will be used in a single cold mass and cryostat for the Q2a and Q2b.

All MQXF magnets will have the same cross-section design, and will be fabricated by a collaboration between CERN and the US-HiLumi Project, a continuation of the LARP Program [4]. A series of short models (1.2 m of magnetic lengths), called MQXFS, and of long prototypes, is currently being fabricated both at CERN and by LARP. The start of the series production, consisting of 16 magnets and 4 spares, is expected to occur in 2018. The "first-generation" magnet parameters were presented in [5]–[13]. Here, we give an update on the development of

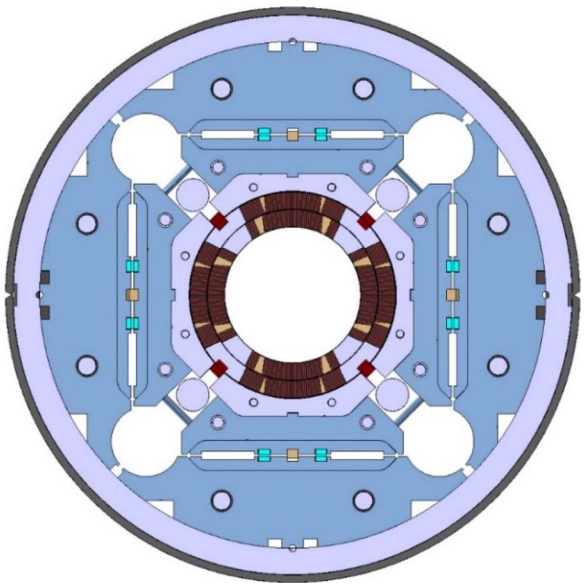

Fig. 1. Cross-section of the Nb_3Sn low-β quadrupole magnet MQXF.

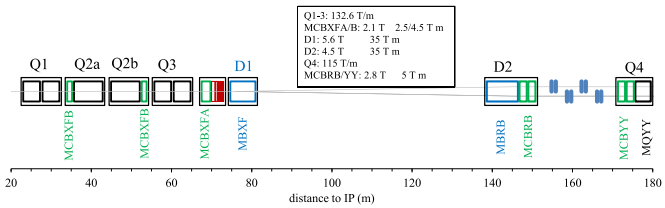

Fig. 2. Schematic view of the layout for the HiLumi interaction regions. Thick boxes indicate magnetic length, thin boxes indicate the cryostat.

MQXF, we describe the changes implemented in the "second generation" design, and we summarize the new parameters.

II. Superconducting Strand and Cable

The cable of MQXF is composed by 40 strands of 0.85 mm diameter, with a Cu/non-Cu ratio of 1.2 and a minimum non-Cu J_c of 2450 (1400) A/mm^2 at 12 (15) T of applied magnetic field and at 4.2 K (see strand specifications in Table I).

During the initial phase of the short model program, three different strand architectures were implemented (see Fig. 3): the RRP 108/127 by Oxford Superconducting Technology (OST), used for LARP coils 01 to 06, the RRP 132/169 by OST for CERN coils 101 to 104, and the PIT 192 from Bruker for CERN coils 201-202. Both the RRP 108/127 and PIT 192 have been selected for the prototype phase. Fig. 4 compares the strand critical current specifications with the values obtained by measurements of RRP strands extracted from the cables used in the coils for the first short model. The samples were reacted with the coils. The heat treatment schedule was the following: 48 h (or 72 h) at 210 °C, 48 h at 400 °C, 50 h at 640 °C. For each coil, we plot only the lowest performing strands. The experimental data, which are fitted with a parameterization curve [14] and include self-field correction, show that the RRP strand properties meet the critical current specifications, with a RRR consistently >150. About 5% lower J_c has been measured

TABLE I
Strand Specifications and Cable Parameters

Parameter	Unit	
Strand diameter	mm	0.85
Sub-element diameter	μm	≤55
Cu/SC		1.2±0.1
RRR		>150
I_c (12 T, 4.2 K), no self-field corr.	A	>632
I_c (15 T, 4.2 K), no self-field corr.	A	>331
Non-Cu J_c (12 T, 4.2 K), no self-field corr.	A/mm^2	>2450
Non-Cu J_c (15 T, 4.2 K), no self-field corr.	A/mm^2	>1280
Number of strands in cable		40
Cable bare width (before/after HT)	mm	18.150/18.363
Cable bare mid-thick. (before/after HT)	mm	1.525/1.594
Cable bare inner-thick. (before/after HT)	mm	1.462/1.530
Cable bare outer-thick. (before/after HT)	mm	1.588/1.658
Cable width expansion during HT	%	1.2
Cable mid-thick. expansion during HT	%	4.5
Keystone angle	Deg.	0.40
Pitch length	mm	109
Cable core width	mm	12
Cable core thickness	μm	25
Cabling degradation	%	<5
Insulation thickness per side at 5 MPa	μm	145±5

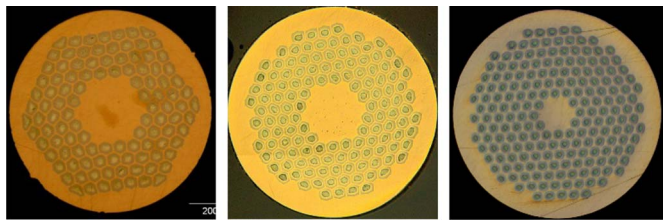

Fig. 3. Superconducting strands used for the MQXF short model program: 108/127 RRP from OST (left), 132/169 RRP from OST (center), 192 PIT from Bruker EAS (right).

on the PIT samples. A detailed overview of the RRP and PIT strand properties and of the development program carried out on the PIT conductor is described in [15].

The bare superconducting cable is 18.150 mm wide and 1.525 mm thick, with a keystone angle of 0.4°. The angle was reduced from the "first-generation" value of 0.55° to bring the critical current degradation due to cabling to < 5% in the PIT conductor and < 3% in the RRP conductor. For the coil design and the field quality computation, an increase of width and mid-thickness of 1.2% and 4.5% respectively was assumed, with the same keystone angle, as observed by dimensional measurements performed on cross-section of first-generation coils [16]. The cable is insulated with braided S2-glass, with a nominal thickness of 145 μm $+ -5$ at a pressure of 5 MPa.

III. Coil Design and Fabrication

The MQXF coils features 50 turns wound in 2 layers around a Ti alloy pole and subdivided in 4 blocks per quadrant (see Fig. 5). The outer layer pole includes a longitudinal slot where a G11 pole alignment key is inserted to provide azimuthal alignment of the coil with respect to the support structure. In addition to holes for pins and screws required for coil

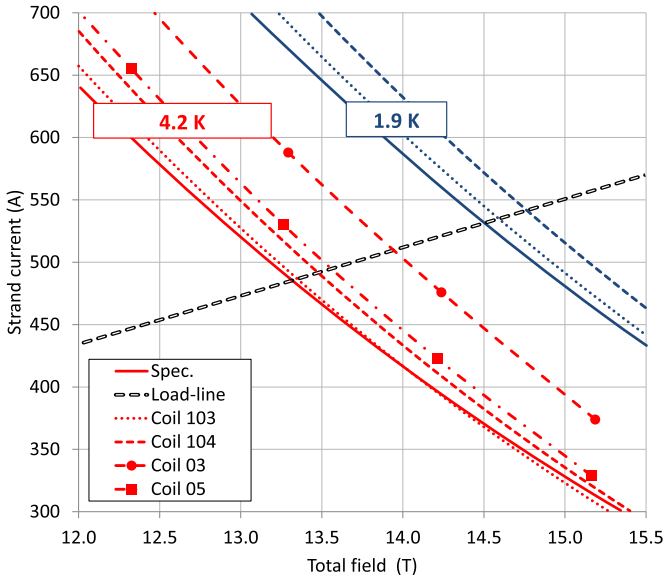

Fig. 4. Strand critical currents versus total magnetic field (including self-field correction): values from strand specifications, and fit curve of measurements performed on extracted strand data from coils 103 and 104.

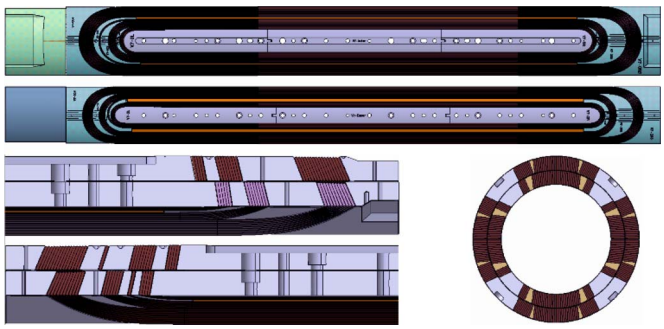

Fig. 5. Design of MQXF short model coil: view from outer radius of outer and inner layer (top), return and lead-end cross-section (bottom left), and straight section cross-section (bottom right).

fabrication and handling, the pole also includes 8 mm diameter holes, 50 mm apart, for cooling purposes.

The top view of the coils and sections of the end in the non-connection side (or return-end) and connection side (or lead-end) side are shown in Fig. 5.

The end turns are separated into two blocks by end-spacers, both in the inner and in the outer layer, to reduce the peak field (about 1% lower than in the straight section) and for field quality optimization (see next section). "Accordion cuts" were applied in the end-shoes and end-spacer design to facilitate their installation during fabrication. 140 mm long end-shoe extensions at the lead ends of both layers protect the area where the Nb-Ti to Nb_3Sn splices are made.

For the short model program, 13 first-generation coils have been fabricated, including a coil wound with Cu cable, and 2 practice coils, which were cut to analyze the quality of impregnation and the conductor positions [16]. LARP coil 02 was tested as a single coil in a "mirror magnet" structure and reached 90% of the maximum current limit. As described in details in [17], for the second-generation coils, presently being

TABLE II
COIL AND MAGNET PARAMETERS

Parameter	Unit	
Coil clear aperture diameter	Mm	150
Magnet (LHe vessel) outer diameter	Mm	630
No. turns in layer 1/2 (octant)		22/28
Operational temperature T_{op}	K	1.9
Magnetic length (Q1-Q3)/(Q2)	M	4.20/7.15
Operational gradient G_{op}	T/m	132.6
Operational current I_{op}	kA	16.47
Operational conductor peak field B_{op}	T	11.4
I_{op}/I_{ss} at 1.9 K	%	77
Stored energy density at I_{op} (Q1-Q3)/(Q2)	MJ/m	1.17
Differential inductance at I_{op}	mH/m	8.21
Stored energy at I_{op} (Q1-Q3)/(Q2)	MJ	4.91/8.37
F_x / F_y (per octant) at I_{op}	MN/m	+2.47/ -3.48
F_ϑ layer1/layer2 (per octant)	MN/m	-1.84/-2.14
F_z (whole magnet) at I_{op}	MN	1.17

fabricated, a fine tuning of the coil cross-section was performed to 1) account for the new cable geometry (new keystone angle and dimensions after reactions), 2) correct the impact of coil mechanical deformation on field quality, 3) optimize harmonics at 123 T/m, a mid-value considering that the operational current in the triplet will be between 90% and 100% of the nominal gradient, depending on the LHC final energy (6.5 or 7 TeV) and on the optics, 4) add S2-glass shims on mid-plane and pole region to control field quality during production, and 5) compensate for the end effects on the integrated harmonics (in combination with minor changes in the end-spacers' design). The same design will be adopted for the prototype coils.

IV. MAGNET PARAMETERS AND MAGNETIC ANALYSIS

The main dimensional and operational parameters of the magnet are summarized in Table II. In the operational conditions, the quadrupole needs to generate at 1.9 K a gradient of 132.6 T/m with a peak field in the conductor of 11.4 T at a current of 16.47 kA.

The reduction of operational gradient with respect to first-generation's 140 T/m was compensated by increasing the magnetic length from 4.00 to 4.20 m for Q1/Q3 and from 6.80 to 7.15 m for Q2a/Q2b. As a result, according to the strand specifications described in the previous section, the operational margin on the load-line $(1 - I_{\mathrm{op}}/I_{\mathrm{ss}})$ increased from 18% to 23%.

Table III describes the estimated field quality of the triplets, at the reference radius of 50 mm. The allowed field harmonics (b_6, b_{10}) are optimized at operational conditions, and are expected to be below 1 unit in absolute value (see integral columns). Contributions from the coil mechanical deformations during assembly and cool-down (computed by a 2-D finite element model and transferred to a 2-D magnetic model [7]), from the iron saturation, and from the coil ends were taken into account and compensated through the straight part [17]. Fine tuning of b_6 will be possible by varying the thickness of shims included in the coil design on the pole and on the mid-plane region. Random components are estimated for a 25 μm random error in the block positioning for non-allowed, and 100 μm

TABLE III
EXPECTED FIELD QUALITY IN THE TRIPLET ($R_{\mathrm{ref}} = 50$ mm)

	Straight part[a]										Ends[b]		Integral			
		Systematic					Uncertainty		Random				Q1/Q3		Q2a/Q2b	
Nor.	Geom.	Mech.	Sat.	Pers.	Inj.	Op.	Inj.	Op.	Inj.	Op.	LE	RE	Inj.	Op.	Inj.	Op.
2									10.000	10.000	0.000	0.000	0.000	0.000	0.000	0.000
3	0.000	0.000	0.000	0.000	0.000	0.000	0.820	0.820	0.820	0.820	0.000	0.000	0.000	0.000	0.000	0.000
4	0.000	0.000	0.000	0.000	0.000	0.000	0.570	0.570	0.570	0.570	0.000	0.000	0.000	0.000	0.000	0.000
5	0.000	0.000	0.000	0.000	0.000	0.000	0.420	0.420	0.420	0.420	0.000	0.000	0.000	0.000	0.000	0.000
6	-2.200	0.900	0.660	-20.000	-21.300	-0.640	1.100	1.100	1.100	1.100	8.943	-0.025	-16.692	0.323	-18.593	-0.075
7	0.000	0.000	0.000	0.000	0.000	0.000	0.190	0.190	0.190	0.190	0.000	0.000	0.000	0.000	0.000	0.000
8	0.000	0.000	0.000	0.000	0.000	0.000	0.130	0.130	0.130	0.130	0.000	0.000	0.000	0.000	0.000	0.000
9	0.000	0.000	0.000	0.000	0.000	0.000	0.070	0.070	0.070	0.070	0.000	0.000	0.000	0.000	0.000	0.000
10	-0.110	0.000	0.000	4.000	3.890	-0.110	0.200	0.200	0.200	0.200	-0.189	-0.821	3.119	-0.175	3.437	-0.148
11	0.000	0.000	0.000	0.000	0.000	0.000	0.026	0.026	0.026	0.026	0.000	0.000	0.000	0.000	0.000	0.000
12	0.000	0.000	0.000	0.000	0.000	0.000	0.028	0.028	0.028	0.028	0.000	0.000	0.000	0.000	0.000	0.000
13	0.000	0.000	0.000	0.000	0.000	0.000	0.009	0.009	0.009	0.009	0.000	0.000	0.000	0.000	0.000	0.000
14	-0.790	0.000	-0.080	1.000	0.210	-0.870	0.023	0.023	0.023	0.023	-0.545	-1.083	0.033	-0.856	0.106	-0.862
Skew	Geom.	Mech.	Sat.	Pers.	Inj.	Op.	Inj.	Op.	Inj.	Op.	LE	RE	Inj.	Op.	Inj.	Op.
2									10.000	10.000	-31.342	0.000	-2.985	-2.985	-1.753	-1.753
3	0.000	0.000	0.000	0.000	0.000	0.000	0.650	0.650	0.650	0.650	0.000	0.000	0.000	0.000	0.000	0.000
4	0.000	0.000	0.000	0.000	0.000	0.000	0.650	0.650	0.650	0.650	0.000	0.000	0.000	0.000	0.000	0.000
5	0.000	0.000	0.000	0.000	0.000	0.000	0.430	0.430	0.430	0.430	0.000	0.000	0.000	0.000	0.000	0.000
6	0.000	0.000	0.000	0.000	0.000	0.000	0.310	0.310	0.310	0.310	2.209	0.000	0.210	0.210	0.124	0.124
7	0.000	0.000	0.000	0.000	0.000	0.000	0.190	0.190	0.190	0.190	0.000	0.000	0.000	0.000	0.000	0.000
8	0.000	0.000	0.000	0.000	0.000	0.000	0.110	0.110	0.110	0.110	0.000	0.000	0.000	0.000	0.000	0.000
9	0.000	0.000	0.000	0.000	0.000	0.000	0.080	0.080	0.080	0.080	0.000	0.000	0.000	0.000	0.000	0.000
10	0.000	0.000	0.000	0.000	0.000	0.000	0.040	0.040	0.040	0.040	0.065	0.000	0.006	0.006	0.004	0.004
11	0.000	0.000	0.000	0.000	0.000	0.000	0.026	0.026	0.026	0.026	0.000	0.000	0.000	0.000	0.000	0.000
12	0.000	0.000	0.000	0.000	0.000	0.000	0.014	0.014	0.014	0.014	0.000	0.000	0.000	0.000	0.000	0.000
13	0.000	0.000	0.000	0.000	0.000	0.000	0.010	0.010	0.010	0.010	0.000	0.000	0.000	0.000	0.000	0.000
14	0.000	0.000	0.000	0.000	0.000	0.000	0.005	0.005	0.005	0.005	-0.222	0.000	-0.021	-0.021	-0.012	-0.012

[a]Magnetic length straight part: Q1/Q3 3.459 m, Q2a/Q2b 6.409 m
[b]Magnetic length ends: lead end 0.400 m, return end 0.341 m

for allowed. The most critical components are low-order harmonics (b_3, a_3, b_4, a_4). To minimize these components we opted for a strategy similar to that used in the RHIC magnets [18], and successfully tested in the HQ03 magnet [19] with magnetic shims to be inserted in the bladder s slot [17]. This allows correcting (I) ± 5 units of b_3; (II) ± 5 units of a_3; (III) ± 3 units of b_4; (IV) ± 1 units of a_4, for a maximum of two harmonics at the same time, through an asymmetric magnetic shimming.

V. SUPPORT STRUCTURE DESIGN AND MECHANICAL ANALYSIS

The coils of MQXF are assembled inside a support structure based on an external aluminum shell pre-loaded with bladders and keys (see Fig. 6). The design was developed in successive stages by the LARP Program [20], [21] and it is basically a scale-up, both in diameter and length, of the HQ structure [22], [23]. An overview of the different components for the MQXFB magnet is shown in Fig. 7. The coils are encased in aluminum collar laminations, 50 mm thick, bolted and locked around a G11 pole key inserted each coil's pole slot [Fig. 7(a)]. The collars and the pole keys provide azimuthal alignment between the coils and the structure without contributing to the coil pre-load. Four iron pads, made of 5.8-mm-thick laminations, are then bolted around the collared coils [Fig. 7(b)]. They include a faceted slot which allows the insertion of the iron master keys ("masters"), full-length trapezoidal plates containing bladders and loading keys. The system of coils, collars, pads and masters constitutes the coil-pack sub-assembly [Fig. 7(c)]. A second sub-assembly is composed by the aluminum shells and the iron yokes. The stacked yoke laminations, 5.8-mm-thick,

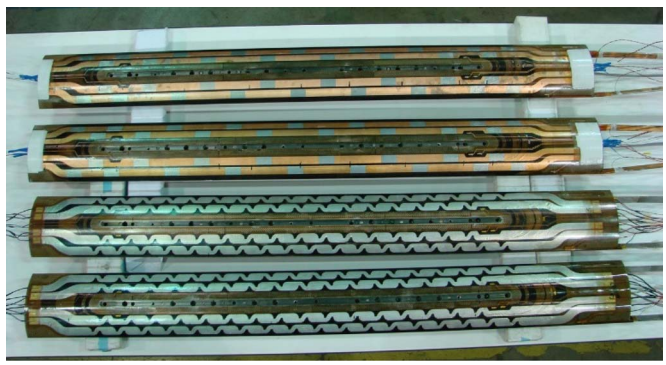

Fig. 6. Coil assembled in the first MQXF short models: from bottom to top, coil 03 and 05 fabricated by LARP) and coil 103 and 104 (fabricated by CERN).

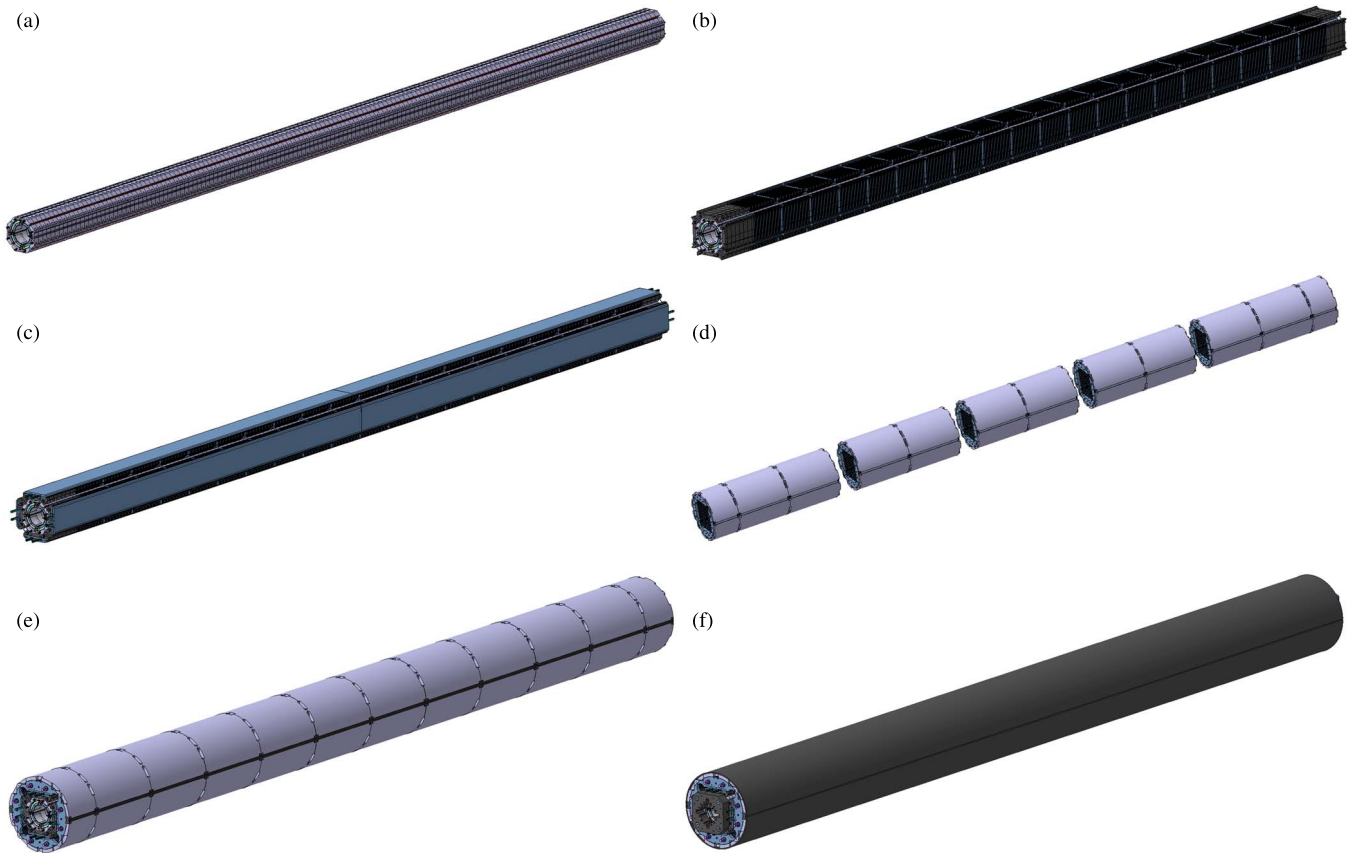

Fig. 7. Components of the MQXFB cold mass: (a) collars, (b) pads, (c) masters, (d) and (e) yoke and shells, (f) LHe vessel and axial loading system.

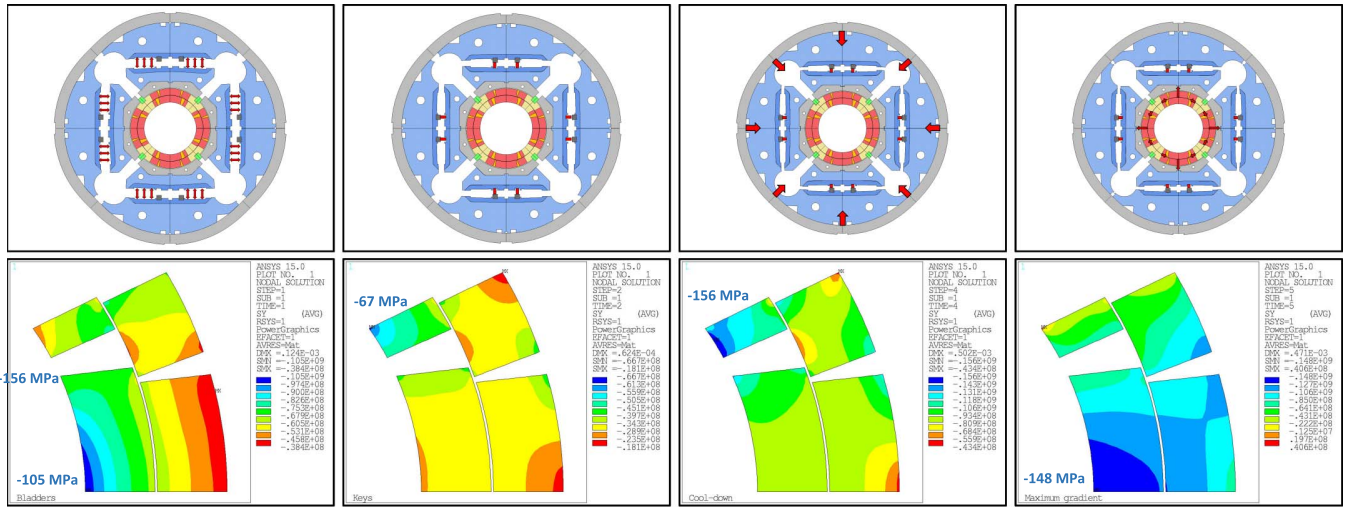

Fig. 8. Loading sequence of MQXF, with deformed shape (top) and coil azimuthal stress (bottom) in MPa. From left to right: bladder operation, key insertion and bladder deflation, cool-down, nominal gradient.

are inserted in a set of 2 or 3 aluminum shells [Fig. 7(d)]; these modules are then combined together with tensioned tie rods to form the yoke-shell sub-assembly. The insertion of the coil-pack in the shell-yoke sub-assembly [Fig. 7(e)], followed by the welding of the stainless steel shells and the mounting of the axial pre-load system, completes the MQXFB cold-mass [Fig. 7(f)]. In the case of MQXFA, two 4.3-m-long magnets are contained within the same stainless steel shell.

A view of the different pre-loading steps, with the deformed shape of the magnet cross-section and the plot of the azimuthal stress in the coil are given in Fig. 8. In the first step, bladders are inserted and inflated to 45 MPa in order to open a gap of about 0.700 mm between the load keys and the master. The gap is then filled with a shim of 0.550 mm (with 0.150 mm of clearance), and then the bladder is deflated and removed. During cool-down, the aluminum shell shrinks and contributes

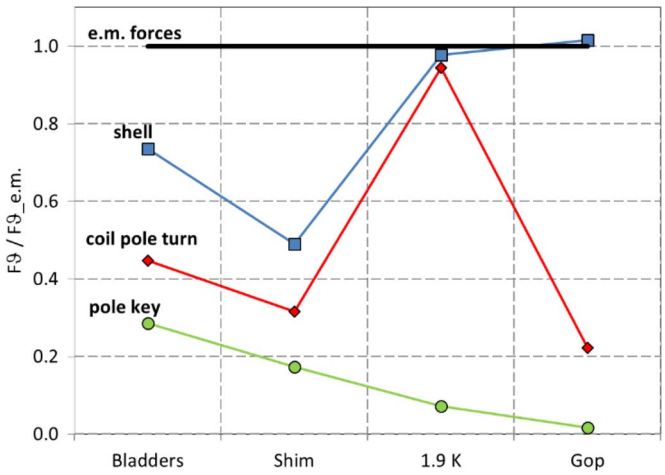

Fig. 9. Ratio between azimuthal total e.m. force per octant (see Table II) and the azimuthal force provided by the shell and received by the coil and pole key.

to the increase of coil pre-load, sufficient to hold the coil pole under compression when the magnet is powered to operational current. In terms of peak stress, the coil reaches a maximum compression of −105 MPa during room temperature bladder operation, −156 MPa in the pole region at 1.9 K, and −148 MPa on the mid-plane with electro-magnetic (e.m.) forces. The same loading sequence is plotted in Fig. 9, this time pointing out how the internal mechanical forces are distributed within the magnet components and how they compare to the e.m. forces. In particular, the markers indicate the ratio between the azimuthal e.m. force per octant (see Table II), and the mechanical azimuthal forces imparted by the shell (in tension), and received by the coil and the pole key (in compression). All the forces are given in absolute value. The graph in Fig. 9 shows that at room temperature, when the bladders are inflated, 65% of the force provided by the shell is transferred to the coil, the rest being intercepted by the pole key. In fact, locked by the collars, the pole key guarantees coil azimuthal alignment of the coil to the structure, "at the expense" of a fraction of the force generated by the bladders. The same fraction is observed when keys are inserted and bladders deflated. At this stage, it can be noted that the force coming from the shell is reduced because of the clearance required to insert the load shims (spring-back).

At 1.9 K, the shell pre-loads the coil to the target value corresponding to the e.m. force, being the force on the pole key significantly reduced. With the e.m. forces, the coil pole turns are still under compression, and the minimal compressive force on the pole key indicates that coil alignment is maintained.

The assembly and loading procedure, as well as the stress level in shell and axial rods, were verified in two short model support structures assembled at CERN and LBNL around aluminum dummy coils (see Fig. 10). Excellent agreement was found between strain gauges mounted on dummy coils, shell and axial rods, and the prediction of the numerical model. A detailed analysis of the results is given in [24].

VI. Quench Protection

The triplet will have two power circuits: one for Q1 and Q3 in series, and the second one for Q2a and Q2b in series. With

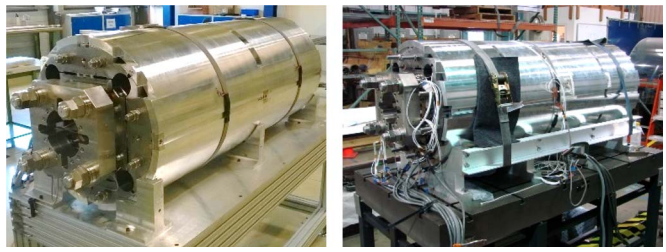

Fig. 10. Two identical MQXF short model support structure assembled around aluminum dummy coils at CERN (left) and at LBNL (right).

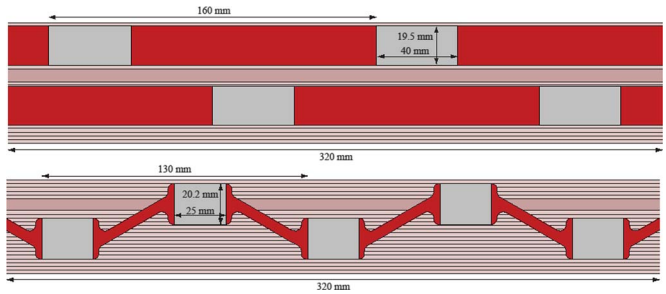

Fig. 11. Inner layer (top) and outer layer (bottom) quench heaters: stainless steel heating stations (gray), and copper plated parts (red).

the stored energy in the coil being 0.08 mJ/mm^3, ∼50% larger than the LHC main dipole, the quench protection of MQXF is particularly challenging. Also, since the circuit inductance is of ∼100 mH, only a ∼5% of the energy can be extracted through a dump resistor. Therefore, one has to rely on quench heaters. MQXF will have quench heaters composed by 25 μm stainless steel strips with a 50 μm polyimide layer (see Fig. 11). In the outer layer (OL), two strips are installed on top of each coil block with heating stations 40 mm long, 20 mm wide, and separated by 120 mm sections with 10 μm copper cladding. In the inner layer (IL), a "zig-zag" shape is employed with heating stations 25 mm long, 20 mm wide, and alternatively covering blocks near the pole and mid-plane turns.

As an attempt to reduce the detachment of the trace from the coil experienced in previous LARP magnets [25], the copper sections are designed to be narrower to maximize the area of perforated polyimide. This solution will be examined after the magnet is tested to determine its efficacy. As an alternative system to replace the inner layer quench heater, the CLIQ system [26]–[28], based on coil heating induced by fast current discharge in the magnet, is also considered. Table IV provides the estimated peak temperature and voltages, assuming 7 ms of detection time to reach the 100 mV threshold, 10 ms of validation time, 5 ms of switch opening, and quench heater delay time of 20–25 ms. The dump resistor is set to be 46 mΩ, with a maximum voltage between ends of 800 V. The peak temperature in the different scenario can be maintained below 350 K, assumed as a safe limit to reduce the risk of permanent degradation. In terms of peak voltages, the maximum values for 1) coil-to-ground with symmetric grounding, 2) turn-to-turn, 3) layer-to-layer and 4) mid-plane to mid-plane are also given in Table IV (for the CLIQ voltage no energy extraction is assumed). Failure scenarios are described in [29].

TABLE IV
QUENCH PROTECTION SYSTEM PARAMETERS AND RESULTS

Parameters	Units			
2 power supply scenario				
Dump resistor (Vmax)	mΩ (V)		46 (800)	
V threshold	mV		100	
Detection time	ms		7	
Validation time	ms		10	
Switch opening time	ms		5	
Hot spot T (K)				
IL-OL quench heaters			257	
OL quench heaters			341	
CLIQ-OL quench heaters			230	
CLIQ			250	
Peak voltages (V)	to gr.	turn-turn	lay-lay	mid-mid
IL-OL quench heaters	659	44	421	313
OL quench heaters	798	81	509	311
CLIQ-OL quench heaters	507	18	497	509
CLIQ	576	24	497	509

VII. CONCLUSION AND PLANS

We have presented an overview of the design of MQXF, the low-β quadrupole magnet under development for the HiLumi project. A second-generation set of parameters were defined. At the time of the submission of this paper, 13 short model coils have been fabricated, four of which have been assembled in the first short model magnet expected to be tested by the end of 2015, and the fabrication of the first long prototype has begun.

REFERENCES

[1] "HL-LHC preliminary design report," Conseil Européen pour la Recherche Nucléaire (CERN), Geneva, Switzerland, CERN-ACC-2014-0300, Nov. 2014.

[2] S. Feher *et al.*, "Production and installation of the LHC low-β triplets," *IEEE Trans. Appl. Supercond.*, vol. 16, no. 2, pp. 437–440, Jun. 2006.

[3] A. Yamamoto *et al.*, "Production and measurement of the MQXA series of LHC low-β insertion quadrupoles," *IEEE Trans. Appl. Supercond.*, vol. 15, no. 2, pp. 1084–1089, Jun. 2005.

[4] S. A. Gourlay *et al.*, "Magnet R&D for the US LHC accelerator research program," *IEEE Trans. Appl. Supercond.*, vol. 16, no. 2, pp. 324–327, Jun. 2006.

[5] E. Todesco *et al.*, "Design studies for the low-beta quadrupoles for the LHC luminosity upgrade," *IEEE Trans. Appl. Supercond.*, vol. 23, no. 3, Jun. 2013, Art. ID 4002405.

[6] E. Todesco *et al.*, "A first baseline for the magnets in the high luminosity LHC insertion regions," *IEEE Trans. Appl. Supercond.*, vol. 24, no. 3, Jun. 2014, Art. ID 4003305.

[7] P. Ferracin *et al.*, "Magnet design of the 150 mm aperture low-β quadrupoles for the high luminosity LHC," *IEEE Trans. Appl. Supercond.*, vol. 24, no. 3, Jun. 2014, Art. ID 4002306.

[8] F. Borgnolutti *et al.*, "Magnetic design optimization of a 150 mm aperture Nb_3Sn low-beta quadrupole for the HiLumi LHC," *IEEE Trans. Appl. Supercond.*, vol. 24, no. 3, Jun. 2014, Art. ID 4000405.

[9] G. Manfreda *et al.*, "Quench protection study of the Nb_3Sn low-β quadrupole for the LHC luminosity upgrade," *IEEE Trans. Appl. Supercond.*, vol. 24, no. 3, Jun. 2014, Art. ID 4700405.

[10] G. Ambrosio, "Nb_3Sn high field magnets for the high luminosity LHC upgrade project," *IEEE Trans. Appl. Supercond.*, vol. 25, no. 3, Jun. 2015, Art. ID 4002107.

[11] S. Izquierdo Bermudez *et al.*, "Coil end optimization of the Nb_3Sn quadrupole for the high luminosity LHC," *IEEE Trans. Appl. Supercond.*, vol. 25, no. 3, Jun. 2015, Art. ID 4001504.

[12] M. Juchno, "Support structure design of the Nb_3Sn quadrupole for the high luminosity LHC," *IEEE Trans. Appl. Supercond.*, vol. 25, no. 3, Jun. 2015, Art. ID 4001804.

[13] V. Marinozzi, "Study of quench protection for the Nb_3Sn low-β quadrupole for the LHC luminosity upgrade (HiLumi-LHC)," *IEEE Trans. Appl. Supercond.*, vol. 25, no. 3, Jun. 2015, Art. ID 4002905.

[14] L. Bottura and B. Bordini, "$J_c(B, T, \varepsilon)$ parameterization for the ITER Nb_3Sn production," *IEEE Trans. Appl. Supercond.*, vol. 19, no. 3, pp. 1521–1529, Jun. 2009.

[15] B. Bordini *et al.*, "Electrical performance of the Nb_3Sn conductor for the HiLumi project," *IEEE Trans. Appl. Supercond.*, submitted for publication.

[16] E. Rochepault *et al.*, "Dimensional changes of Nb_3Sn Rutherford cables during heat treatment," *IEEE Trans. Appl. Supercond.*, submitted for publication.

[17] S. Izquierdo Bermudez *et al.*, "Second generation coil design of the Nb_3Sn low-β quadrupole for the high luminosity LHC," *IEEE Trans. Appl. Supercond.*, submitted for publication.

[18] R. Gupta *et al.*, "Tuning shims for high field quality in superconducting magnets," *IEEE Trans. Magn.*, vol. 32, no. 4, pp. 2069–2073, Jul. 1996.

[19] J. DiMarco *et al.*, "Test results of the LARP HQ03a Nb_3Sn quadrupole," *IEEE Trans. Appl. Supercond.*, submitted for publication.

[20] S. Caspi *et al.*, "Design and analysis of TQS01, a 90 mm Nb3Sn model quadrupole for LHC luminosity upgrade based on a key and bladder assembly," *IEEE Trans. Appl. Supercond.*, vol. 16, no. 2, pp. 358–361, Jun. 2006.

[21] P. Ferracin *et al.*, "Fabrication and test of a 3.7 m long support structure for the LARP Nb_3Sn quadrupole magnet LQS01," *IEEE Trans. Appl. Supercond.*, vol. 19, no. 3, pp. 1683–1686, Jun. 2009.

[22] S. Caspi *et al.*, "Design of HQ—A high field large bore Nb_3Sn quadrupole magnet for LARP," *IEEE Trans. Appl. Supercond.*, vol. 19, no. 3, pp. 1235–1238, Jun. 2009.

[23] S. Caspi *et al.*, "Design of a 120 mm bore 15 T quadrupole for the LHC upgrade phase II," *IEEE Trans. Appl. Supercond.*, vol. 20, no. 3, pp. 144–147, Jun. 2010.

[24] M. Juchno *et al.*, "Mechanical qualification of the support structure for MQXF, the Nb_3Sn low-β quadrupole for the high luminosity LHC," *IEEE Trans. Appl. Supercond.*, submitted for publication.

[25] G. Ambrosio *et al.*, "Test results of the first 3.7 m long Nb_3Sn quadrupole by LARP and future plans," *IEEE Trans. Appl. Supercond.*, vol. 21, no. 3, pp. 1858–1862, Jun. 2011.

[26] E. Ravaioli *et al.*, "New coupling loss induced quench protection system for superconducting accelerator magnets," *IEEE Trans. Appl. Supercond.*, vol. 24, no. 3, Jun. 2014, Art. ID 0500905.

[27] E. Ravaioli *et al.*, "Protecting a full-scale Nb3Sn magnet with CLIQ, the new coupling-loss induced quench system," *IEEE Trans. Appl. Supercond.*, vol. 25, no. 3, Jun. 2015, Art. ID 4001305.

[28] E. Ravaioli *et al.*, "Advanced quench protection for the Nb3Sn quadrupoles for the high luminosity LHC," *IEEE Trans. Appl. Supercond.*, submitted for publication.

[29] V. Marinozzi *et al.*, "Quench protection study of the updated MQXF for the LHC luminosity upgrade (HiLumi LHC)," *IEEE Trans. Appl. Supercond.*, submitted for publication.